

# Ascending aortic aneurysm in angiotensin II- infused mice: formation, progression and the role of focal dissections

Running title: Ascending aortic aneurysm in Ang II- infused mice

Bram Trachet<sup>1,2</sup>, Alessandra Piersigilli<sup>3,4</sup>, Rodrigo A. Fraga-Silva<sup>1</sup>, Lydia Aslanidou<sup>1</sup>, Jessica Sordet-Dessimoz<sup>5</sup>, Alberto Astolfo<sup>6</sup>, Marco F.M. Stampanoni<sup>6,7</sup>, Patrick Segers<sup>2</sup>, Nikolaos Stergiopoulos<sup>1</sup>

<sup>1</sup> Institute of Bioengineering, Ecole Polytechnique Fédérale de Lausanne, Lausanne, Switzerland

<sup>2</sup> IBiTech - bioMMeda, Ghent University-iMinds Medical IT, Ghent, Belgium

<sup>3</sup> School of Life Sciences, PTEC GE, Ecole Polytechnique Fédérale de Lausanne, Lausanne, Switzerland

<sup>4</sup> Institute of Animal Pathology, Vetsuisse Faculty, University of Bern, Bern, Switzerland

<sup>5</sup> Histology Core Facility, Ecole Polytechnique Fédérale de Lausanne, Lausanne, Switzerland

<sup>6</sup> Swiss Light Source, Paul Scherrer Institut, Villigen, Switzerland

<sup>7</sup> Institute for Biomedical Engineering, University and ETH Zürich, Zürich, Switzerland

Keywords : aortic dissection, aortic aneurysm, ascending aorta, mouse models of human disease, cardiovascular imaging

TOC: basic science, vascular biology

Manuscript: 5962 words, 6 Figures

Supplementary material: 2 Figures, 2 Tables

Bram Trachet

LHTC STI IBI EPFL  
BM 5128 Station 17  
CH-1015 Lausanne (Switzerland)

Tel: +41 21 693 83 81

[bram.trachet@epfl.ch](mailto:bram.trachet@epfl.ch)

33  
34  
35  
36  
37  
38  
39  
40  
41  
42  
43  
44  
45  
46  
47  
48  
49  
50  
51  
52  
53  
54  
55  
56  
57

This is a pre-copyedited, author-produced PDF of an article accepted for publication in ATVB following peer review.

The version of record is available online at:

*Ascending aortic aneurysm in angiotensin II infused mice: formation, progression and the role of focal dissections*

Bram Trachet; Alessandra Piersigilli; Rodrigo A. Fraga-Silva; Lydia Aslanidou, Jessica Sordet-Dessimoz, Alberto Astolfo, Marco FM Stampanoni, Patrick Segers and Nikolaos Stergiopoulos

Arteriosclerosis, Thrombosis and Vascular Biology 2016, 36, 673-681

<https://doi.org/10.1161/ATVBAHA.116.307211>

## 58 **Abstract**

59

60 **Objective.** To understand the anatomy and physiology of ascending aortic  
61 aneurysms in angiotensin II-infused ApoE<sup>-/-</sup> mice.

62 **Approach and results.** We combined an extensive in vivo imaging protocol (high-  
63 frequency ultrasound and contrast-enhanced micro-CT at baseline and after 3, 10, 18  
64 and 28 days of angiotensin II infusion) with synchrotron-based ultra-high resolution  
65 ex vivo imaging (phase contrast X-Ray tomographic microscopy) in n=47 angiotensin  
66 II-infused mice and 6 controls. Aortic regurgitation increased significantly over time,  
67 as did the luminal volume of the ascending aorta. In the samples that were scanned  
68 ex vivo we observed one or several focal dissections, with the largest located in the  
69 outer convex aspect of the ascending aorta. The volume of the dissections  
70 moderately correlated to the volume of the aneurysm as measured in vivo ( $r^2=0.46$ ).  
71 After 3 days of angiotensin II infusion we found an interlaminal hematoma in 7/12  
72 animals, which could be linked to an intimal tear. There was also a significant  
73 increase in single laminal ruptures, which may have facilitated a progressive  
74 enlargement of the focal dissections over time. At later time points the hematoma  
75 was resorbed and the medial and adventitial thickness increased. Fatal transmural  
76 dissection occurred in 8/47 mice at an early stage of the disease, before adventitia  
77 remodeling.

78 **Conclusions.** We visualized and quantified the dissections that lead to ascending  
79 aortic aneurysms in angiotensin II-infused mice and provided unique insight into the  
80 temporal evolution of these lesions.

81

## 82 **Abbreviations**

83 AAA: Abdominal aortic aneurysm

84 TAA: Thoracic aortic aneurysm

85 PCXTM: Phase Contrast X-ray Tomographic Microscopy

86 ApoE: Apolipoprotein E

87 2D: two-dimensional

88 3D: three-dimensional

89 Micro-CT: micro computed tomography

90 MMode: Motion mode

91 BMode: Brightness mode

92 SR: Sirius Red

93

94

## 95 Introduction

96 Aortic aneurysm is clinically defined as a local increase in aortic diameter of at least  
97 50 % compared to the normal diameter<sup>1</sup>. Abdominal aortic aneurysms (AAA) are  
98 associated with cardiovascular risk factors such as smoking, age, male gender,  
99 hyperlipidemia, hypertension and chronic obstructive pulmonary disease<sup>2</sup>. Although  
100 these factors also underlie the majority of thoracic aortic aneurysms (TAA), the latter  
101 subgroup incidence is more often related to family history than to the above  
102 mentioned factors<sup>3</sup>. Since most aneurysms remain asymptomatic until – often fatal –  
103 complications such as rupture occur, our understanding of the pathogenesis,  
104 especially in early stages, is limited. Angiotensin II infusion into hypercholesterolemic  
105 ApoE<sup>-/-</sup> mice is a well-known experimental model of both AAAs<sup>4</sup> and TAAs<sup>5</sup>. We  
106 have recently explored a novel imaging technique, Phase Contrast X-ray  
107 Tomographic Microscopy (PCXTM), to visualize the abdominal lesions of angiotensin  
108 II-infused mice<sup>6</sup>. Since the axial resolution of our PCXTM scans (6.5 μm) was close  
109 to the thickness of histological coupes for routine morphologic evaluation (4 μm), we  
110 introduced PCXTM-guided histology to select sections of the aorta in a highly precise  
111 manner for pathology analysis<sup>6</sup>. This approach allowed us to demonstrate that the  
112 abdominal lesions in these mice stem from medial ruptures in the suprarenal side  
113 branches, leading to media-adventitia dissection with intramural bleeding and  
114 thrombus formation<sup>6</sup>.

115 Much like in humans, data on TAAs are scarcer than data on AAAs in mouse models.  
116 Daugherty *et al.* reported dilatation of the ascending aorta as semi-quantified on  
117 histological sections after 28 days of continuous angiotensin II infusion in ApoE<sup>-/-</sup>  
118 mice<sup>5</sup>. They observed expansion of inter-laminar spaces, collagen deposition and  
119 macrophage accumulation. The latter changes were found most extensively within  
120 the adventitia while destruction of elastic fibers was observed on the outer convex  
121 aspect of the arch. Luminal dilatation<sup>7-9</sup>, wall thickening<sup>8,9</sup> and elastin fragmentation  
122<sup>8,9</sup> after 28 days of angiotensin II infusion were confirmed by other authors as well.  
123 Rateri *et al.* reported a significant increase in diameter of the ascending aorta within 5  
124 days using 2D high-frequency ultrasound. They also reported interlaminar  
125 hemorrhage at early time points<sup>9</sup>. Furthermore they consistently observed mural  
126 medial breaks within the anterior aspects of the aorta<sup>9</sup>. Although detailed research  
127 on morphology, topography and translational aspects of these ascending aorta  
128 lesions is still lacking, the mouse model is a common and convenient tool in pre-  
129 clinical pharmacological<sup>10-13</sup> and/or gene therapy<sup>14</sup> studies.

130 In the current manuscript, we combined in vivo imaging with PCXTM and PCXTM-  
131 guided histology to visualize, characterize and quantify the lesions in the ascending  
132 aorta of angiotensin II-infused ApoE<sup>-/-</sup> mice. We performed a longitudinal study with  
133 sacrifices at different time points, hence stages of disease development. A large  
134 number of lesions, particularly those found at the earliest time points, did not qualify  
135 as ascending aortic aneurysms from the patho-morphological point of view (not all  
136 layers were involved) nor the clinical point of view (no sufficient increase in lumen  
137 size). The study of these premature lesions with both established and novel  
138 technologies enabled us to present remarkable insights into the pathophysiology and  
139 morphology of murine ascending aortic aneurysms over time.

140

141 **Materials and Methods**

142 Materials and Methods are available in the online-only Data Supplement.

143

## 144 **Results**

### 145 *Aortic dimensions and aortic regurgitation*

146 Using the clinical criterion of an increase in aortic size of 50%, 1/22 cases measured  
147 with MMode, 3/27 cases measured with BMode and 5/11 cases measured with  
148 micro-CT could be diagnosed with an ascending aortic aneurysm (comparing for  
149 each technique the aortic size at the latest available time point to the aortic size at  
150 baseline, in the animals that were scanned successfully at least twice). The  
151 ascending aorta diameter as measured with MMode (1D) increased significantly over  
152 time, but a statistically significant difference was only detected between baseline and  
153 day 28 (Figure 1e, Table I). The aortic area as measured with longitudinal BMode  
154 (2D) and contrast-enhanced micro-CT (3D) increased highly significantly over time  
155 ( $p < 0.001$ ) and differences were significant in between intermediate time points as  
156 well (Figure 1f-g, Table I). Aortic regurgitation as quantified from pulsed Doppler  
157 measurements was present but very low at baseline (day 0), and was significantly  
158 higher than baseline from day 10 on (Figure 1h, Table I).

### 159 *Wall strain and thickness*

160 Circumferential Green-Lagrange strain decreased significantly over time ( $p < 0.001$ ). A  
161 sharp decrease occurred between baseline and day 3, after which the strain values  
162 stabilized (Figure 2b, Table I). Both intima-media thickness and adventitial thickness  
163 as measured on SR-Miller stains were significantly different between angiotensin II-  
164 infused mice and controls (Table I). The medial thickness only reached a significant  
165 difference after 28 days (Figure 2c) while the adventitial thickness was already  
166 significantly different from saline-infused controls at day 10 (Figure 2d). There was  
167 also a trend for increased collagen content in the wall ( $p = 0.51$ , Table I, Figure 2e).

### 168 *Focal dissections in the ascending aorta*

169 In  $n = 41/42$  scanned samples the ex vivo PCXTM images revealed at least 1 and  
170 maximum 4 dissections, defined as “gaps” in the aortic wall of at least 10% of the  
171 local wall thickness (Figure 3a). The geometric mean of the dissection length was  
172 1.07 mm per sample [95% CI: 0.81 – 1.41], its wall surface area was 0.97 mm<sup>2</sup> [95%  
173 CI: 0.65 – 1.46] and its wall volume was 0.022 mm<sup>3</sup> [95% CI: 0.013 – 0.037]. No  
174 dissections were observed in control animals. While the largest dissections occurred  
175 at the latest time points, no significant difference in lesion volume was observed  
176 between the investigated time points of angiotensin II infusion (Figure 3b, Table I).  
177 There was a significant difference in dissection incidence and dissection size in  
178 between circumferential quadrants. The lowest number of dissections occurred on  
179 the inner convex aspect of the aorta, with pairwise comparisons being significant  
180 between the inner convex and right aspects (Figure 3c, Table II). The largest  
181 dissections occurred on the outer convex quadrant of the aorta, with pairwise  
182 comparisons being significant between the outer convex and left quadrants (Figure  
183 3c, Table I). The volume of the ascending aorta as measured with micro-CT prior to  
184 sacrifice (Figure 1c - red) correlated moderately ( $r^2 = 0.46$ ) with the volume of the  
185 dissections (Figure 3a - orange, Figure 3d).

186 The dissections were characterized on image-guided histology by a loss of continuity  
187 in at least three adjacent inner elastic laminae of the tunica media (Figure 4a, 4c).  
188 Applying the morpho-pathological criterion for an aneurysm (i.e. a vascular outpouch

189 involving all layers of the wall <sup>15</sup>) one could state that only 54% of the investigated  
190 stains that showed (part of) a dissection had developed a true ascending aortic  
191 aneurysm (Figure 4b). Apoptosis of smooth muscle cells was most outspoken at the  
192 latest time points and at the edges of the dissection (Figure 1a). The remaining, intact  
193 segments of the vessel did not exhibit evidence of ongoing apoptosis.

#### 194 *Interlaminar microhemorrhage*

195 H&E stained sections showed that interlaminar microhemorrhages and hematomas  
196 occurred after 3 days of angiotensin II infusion (Figure 5a). The hematoma size as  
197 measured on HE stains was larger after 3 days of angiotensin II infusion than at  
198 subsequent time points, indicating this lesion to be an early step in the pathogenesis  
199 of aneurysms in mice (Figure 5c, Table I). The accumulation of extraluminal free  
200 erythrocytes occurred more frequently in the outer (abluminal) laminae (L4 – L7); no  
201 hematoma was found in the inner two laminae (L1 – L2) (Figure 5d, Table II).  
202 Hemosiderophages, stained with Prussian blue, were seen resorbing the hematoma  
203 at later time points (Figure 1b). These observations were confirmed on the 3D  
204 PCXTM images of the animals that had been scanned with contrast-enhanced micro-  
205 CT (Figure 5b). The incidence of extraluminal, intramural Extron leakage was  
206 significantly higher after 3 days of angiotensin II infusion than for controls, but at later  
207 time points the difference was no longer significant (Figure 5e, Table I).

#### 208 *Elastic Laminae ruptures*

209 The combined SR-Miller stained slides revealed several discrete discontinuities in the  
210 medial (elastic) laminae (Figure 6a). Laminar ruptures were present in all animals  
211 (Figure 6b, Table II). The total number of laminar ruptures was significantly higher in  
212 angiotensin II-infused animals than in controls (Table I). The difference reached  
213 significance after 18 days of Ang II infusion (Figure 6b). Neither the incidence nor the  
214 number of ruptures varied in between different quadrants (Figure 6c, Table I, II).  
215 However, both the incidence and the number of ruptures were significantly different in  
216 between layers. The highest number of laminar ruptures occurred in the central  
217 laminae (L2 – L4) while the outer laminae (L1, L7) were less frequently affected  
218 (Figure 6d, Table I, II).

#### 219 *Transmural dissection*

220 All of the 8 animals that were found dead in their cage with hemothorax had died  
221 between 3 and 8 days of angiotensin II infusion, during the initial stage of disease  
222 development. Six out of these eight ascending aortic samples were scanned ex vivo  
223 with PCXTM. In all 6 cases the cause of death could be related to a hemothorax,  
224 secondary to the transmural dissection of the ascending aortic wall. PCXTM-guided  
225 histology confirmed a complete rupture of all laminae in the tunica media. The  
226 transmural dissection ran in the cranial direction (towards the aortic root), be it on the  
227 inner convex aspect (Figure 1Ia) or on the outer convex aspect (Figure 1Ic) of the  
228 aorta.

229

## 230 Discussion

### 231 *In vivo and ex vivo imaging: interpreting the observations*

232 To the best of our knowledge our ex vivo PCXTM images are the first report of  
233 volume and location of the focal dissections that cause ascending aortic aneurysms  
234 in angiotensin II-infused mice. Despite the focal and asymmetric nature of the wall  
235 damage observed ex vivo, an asymmetric outpouch with luminal expansion was not  
236 observed in vivo with BMode or micro-CT. Nevertheless the luminal volume observed  
237 with micro-CT just prior to sacrifice correlated moderately with the size of the focal  
238 dissections observed with PCXTM ( $r^2= 0.46$ , Figure 3d). Since the size of the  
239 dissections was quantified in the absence of intra-aortic pressure, this correlation  
240 does not account for the impact of the dissection on the structural properties and  
241 strain of the aorta. Moreover the size of the aneurysm might also be influenced by  
242 wall remodeling (Figure 2), intramural hematoma formation (Figure 5) and discrete  
243 laminar ruptures (Figure 6), all of which affect the entire wall and not just the region of  
244 the dissection. Considering these confounding factors we believe that a correlation of  
245  $r^2= 0.46$  is not insignificant, and that our data support a (possibly indirect) relationship  
246 between the size of the observed dissections and the size of the aneurysm in vivo.

247  
248 Within the different in vivo imaging techniques, the increased accuracy and added  
249 information of 2D BMode and especially 3D micro-CT resulted in more overt, more  
250 gradual and more significant differences in between different time points than what  
251 was obtained with 1D MMode (Figure 1e-g, Table I). Our data thus contradict earlier  
252 findings of Rateri et al, who observed a more gradual increase with 1D MMode than  
253 with 2D BMode while their BMode measurements reached a plateau value after 7  
254 days of angiotensin II infusion<sup>9</sup>. Moreover 3D imaging enabled us to identify  
255 aneurysms that were not picked up by 2D, and 2D imaging was more sensitive than  
256 1D. Since 1D and 2D ultrasound strongly depend on the field of view chosen by the  
257 user<sup>16</sup>, these findings indicate that for follow-up studies on aneurysm formation 3D  
258 images should be acquired when possible.

259 Both aortic regurgitation and ascending aortic volume were significantly increased  
260 after 10 days of angiotensin II infusion (Figure 1g-h). This leads to a dilemma that  
261 has also been discussed in a clinical context: did the dilatation of the aorta cause the  
262 regurgitation or vice versa?<sup>17, 18</sup>. On the one hand, the fast progression of the  
263 disease (both variables were already increased, albeit not significantly, after 3 days)  
264 seems to suggest that in angiotensin II-infused mice diastolic regurgitation was the  
265 consequence rather than the cause of aortic dilatation, most likely driven by poor  
266 leaflet coaptation<sup>19</sup>. On the other hand, once present, diastolic backflow and the  
267 subsequent hemodynamic perturbations might have played an important role in the  
268 further degeneration of the wall<sup>20</sup>. This is further supported by the fact that the  
269 volume of the dissections was larger in the most convex aspect of the aorta (Figure  
270 3c). Aortic regurgitation has been reported to induce aortic remodeling in the outer  
271 convex aspect of the ascending aorta in pigs<sup>21</sup>. In human patients with a bicuspid  
272 valve, aortic expansion<sup>22</sup> and extracellular matrix protein expression<sup>17</sup> were also  
273 increased in the most convex part of the ascending aorta. The latter might thus be a  
274 “locus minoris resistentiae” to hemodynamic alterations. Follow-up research is  
275 needed to provide more insight into the intriguing role of aortic regurgitation in this  
276 mouse model.



277 *Image-guided histology: exploring potential mechanisms*

278 Since the paraffin cutting (prior to staining) was guided by the PCXTM images, we  
279 were able to target the exact region of interest within each analyzed lesion. The  
280 analysis of this image-guided histology revealed significant differences between early  
281 and late time points of angiotensin II infusion.

282 We observed large intramural hematomas after only 3 days of angiotensin II infusion  
283 (Figure 5). The presence of Exitron aggregates within the wall (Exitron is the micro-  
284 CT contrast agent that had been injected in vivo) indicates an intra vitam locally  
285 increased permeability of the vessel wall, or even loss of continuity of the endothelial  
286 lining<sup>6</sup>. In contrast to Rateri et al, who could not identify any access point for the  
287 interlaminal hematoma<sup>9</sup>, PCXTM (Figure 5b) and PCXTM-guided histology (Figure  
288 4a - day 3) allowed us to visualize the intimal defect which led to a mural bleeding at  
289 these early time points.

290 We also found an increase in laminal ruptures in the tunica media at an early stage  
291 of the disease (Figure 6). Since these laminal ruptures were highly frequent in the 2<sup>nd</sup>  
292 and 3<sup>rd</sup> lamina (Figure 6d), both of which were affected in all focal dissections (Figure  
293 4b), one might hypothesize that the dissections were the result of a progressive tear  
294 that had been initiated by a combination of single laminal ruptures. This theory is  
295 further supported by the anecdotal observation that 7/41 focal dissections occurred in  
296 bilateral pairs, with a tear on the right side of the aorta accompanied by a mirroring  
297 one on the left (e.g. Figure 3a, day 10-18 and Figure 4a, day18). If several laminal  
298 ruptures culminate into a dissection on one side (left or right) this might locally  
299 elongate the aorta and increase the tension on the other side, thus leading to  
300 additional laminal ruptures on that side and an ipsilateral, symmetric dissection.

301  
302 Since apoptosis was mainly observed at later time points and near the edge of  
303 dissections (Figure 1a), it may have played an important role in the progressive  
304 enlargement of the lesion over time, rather than being an early event as widely  
305 assumed<sup>23</sup>. The progression over time of an initially small tear could also be driven  
306 by mechanical forces and factors such as the loss of recoil of adjacent intact elastic  
307 laminae, the focal loss of vessel wall compliance (as evidenced by a decrease in  
308 circumferential strain, Figure 2b) and interlaminal bleeding (Figure 5).

309  
310 After the initial events, further degradation occurred and medial elements were  
311 replaced by the deposition of collagen in response to hematoma organization and  
312 remodeling of the vessel wall (Figure 2a). Since the medial thickness did not change  
313 much after day 10 (Figure 2c) we hypothesize that the formation of granulation tissue  
314 (at first) and fibrosis (later on) were counterbalanced by compensatory hypertrophy  
315 and/or hyperplasia of the remaining medial smooth muscle cells. This could trigger a  
316 vicious circle of degeneration, loss and switch of the contractile phenotype for a  
317 secretory one<sup>24</sup>. The altered physical properties of the wall possibly predisposed  
318 other sectors of the segment to undergo degenerative medial changes as well.

319  
320 We believe that the changes in the adventitia were the result of a combined effect of  
321 (i) systemic angiotensin II-induced vessel fibrosis<sup>25</sup> and (ii) local reinforcement of the  
322 adventitia near focal dissections, in order to prevent transmural dissection due to the  
323 locally weakened tunica media. The latter is further supported by the fact that all fatal  
324 transmural dissections occurred after  $4.6 \pm 1.8$  days of angiotensin II infusion (Figure

325 II), when adventitial remodeling was still at a premature stage (Figure 2d-e). A  
326 transmural dissection may have occurred in those cases where the focal dissection  
327 evolved too abruptly, so that the outer wall segments (which did not have the time to  
328 remodel) could not bear the increased load.

329

### 330 *Translational value of the mouse model*

331 Our previously published PCXTM findings discussed morphological differences  
332 between dissecting AAAs in angiotensin II-infused mice and AAAs observed in  
333 humans<sup>6</sup>. The focal and partial dissections of the tunica media that we report here  
334 have, to the best of our knowledge, never been reported in humans. However, ex  
335 vivo images that visualize the entire ascending aortic wall in 3D with a superior  
336 resolution are difficult (if not impossible) to obtain in a clinical context. Therefore final  
337 conclusions about the translational value of the ascending aneurysms in this mouse  
338 model are premature at this stage.

339

340 An important difference between mice and men is the number of laminae in the  
341 tunica media ( $\pm 7$  in mice,  $\pm 50$  in humans<sup>26</sup>). Wolinsky and Glagov stated that the  
342 tension per lamellar unit is constant ( $2 \text{ N m}^{-1}$ ) among species<sup>27</sup>, but this was later  
343 disputed by Shadwick<sup>28</sup>. Hence the tension on each lamina might be higher in mice.  
344 Also, in mice a rupture in one lamina will have a greater impact on the local load-  
345 bearing capacity, and the tension on the remaining laminae will be higher. This might  
346 explain the observed focal nature of the dissections in mice, and the fast evolution of  
347 the disease compared to humans. A detailed computational analysis would be  
348 necessary to confirm this hypothesis<sup>29</sup>.

349

### 350 *Limitations and future work*

351

352 In this study baseline measurements (prior to pump implantation) were used as  
353 controls for in vivo experiments (ultrasound, micro-CT) while saline-infused ApoE<sup>-/-</sup>  
354 mice were used as controls for the ex vivo experiments (PCXTM, histology). We did  
355 not investigate the influence of hyperlipidemia on ascending aortic aneurysm  
356 formation in this mouse model, and we did not use age-matched controls. These  
357 choices were based on the 3R principle (reducing the number of experimental  
358 animals as much as possible), and on previous studies reporting negative controls at  
359 different time points<sup>8, 9, 13</sup>. Nevertheless, we cannot completely exclude the possibility  
360 that the inclusion of normolipidemic mice and/or age-matched controls would have  
361 affected the conclusions of our work.

362 We could not find an unequivocal explanation as to why the hematoma was restricted  
363 to the outer laminae. We hypothesize that an interstitial outward pressure gradient  
364 might be present within the tunica media. Nevertheless, we cannot exclude the  
365 possibility that the hematoma was not just caused by an intimal tear, and that  
366 additional breaches exist in the outer layers. This theory is supported by the fact that  
367 in 3/42 scanned samples a focal hematoma was detected at the level of the aortic  
368 arch. Since there was no intimal tear in these cases, these hematomas possibly  
369 originated from ruptured vasa vasorum in the outer laminae of the tunica media  
370 (Figure IIc).

371 While the largest dissections were found at the latest time point, we did not find a  
372 statistically significant increase in dissection size over time. The reason is that a  
373 considerable number of animals only suffered from small dissections (Figure 3b)  
374 and/or less prominent adventitial remodeling (Figure 2d-e). A similar variability in size  
375 and timing of the lesions have previously been observed in dissecting AAAs in this  
376 mouse model<sup>30</sup>. This is relatively surprising given the homogeneity of the genetic  
377 background in inbred mice and the identical environmental and experimental  
378 conditions, and may be related to epigenetic heterogeneity and/or differences in local  
379 hemodynamics. Such factors should be taken into account and if possible further  
380 elucidated for future studies to empower this model.

381 *Conclusions*

382 We investigated the pathogenesis of ascending aortic aneurysms in angiotensin II-  
383 infused mice by longitudinal in vivo monitoring as well as ex vivo synchrotron-based  
384 imaging and image-guided histology of the vessel. We visualized how the  
385 axisymmetric increase in luminal size that was measured in vivo was related to highly  
386 non-symmetric focal dissections within the aneurysm wall, and explored potential  
387 disease mechanisms. These novel insights into the morphologic pathology of the  
388 aortic wall in ascending aneurysms of angiotensin II-infused mice will help to interpret  
389 treatment studies using this mouse model, both prospectively and retrospectively.

390

## 391 **Acknowledgments**

392 The authors would like to thank Dr. Pablo Villanueva, Dr. Orestis Vardoulis, Dr.  
393 Carole Van der Donckt and Bieke Vanderveken for their assistance during the  
394 PCXTM scans. Further we wish to acknowledge Agnès Hautier and the entire team  
395 of the Histology Core Facility at EPFL for their technical expertise with the PCXTM-  
396 guided histology, and José Artacho from the Bioimaging and Optics platform at EPFL  
397 for his help with the image data acquisition. We also thank Marion Varet, Celine  
398 Waldvogel and the entire team of the Phenotyping Unit in the Center of  
399 PhenoGenomics at the school of Life Sciences in EPFL for  
400 their technical and scientific expertise in the micro-CT experiments. Finally we thank  
401 Dr. Philippe Jacquet of the Statistics Core Facility at EPFL for his expert help in  
402 organizing the data and Dr. Massimiliano Mariani and Dr. Julie De Backer for their  
403 clinical input and revision of the manuscript.

## 404 **Sources of funding**

405 This research was funded by the Special Research Fund of Ghent University and by  
406 internal funds of the Laboratory of Hemodynamics and Cardiovascular Technology,  
407 EPFL.

## 408 **Disclosures**

409 None.

410

411

412 ,

413

414

415 **References**

416 1. Alexander JJ. The pathobiology of aortic aneurysms. *J. Surg. Res.* 2004;117:163-175  
417 2. Sakalihasan N, Limet R, Defawe OD. Abdominal aortic aneurysm. *Lancet.*  
418 2005;365:1577-1589  
419 3. Coady MA, Davies RR, Roberts M, Goldstein LJ, Rogalski MJ, Rizzo JA, Hammond  
420 GL, Kopf GS, Elefteriades JA. Familial patterns of thoracic aortic aneurysms. *Arch.*  
421 *Surg.* 1999;134:361-367  
422 4. Daugherty A, Manning MW, Cassis LA. Angiotensin ii promotes atherosclerotic  
423 lesions and aneurysms in apolipoprotein e-deficient mice. *J. Clin. Invest.*  
424 2000;105:1605-1612  
425 5. Daugherty A, Rateri DL, Charo IF, Owens AP, Howatt DA, Cassis LA. Angiotensin ii  
426 infusion promotes ascending aortic aneurysms: Attenuation by ccr2 deficiency in  
427 apoe<sup>-/-</sup> mice. *Clinical science (London, England : 1979).* 2010;118:681-689  
428 6. Trachet B, Fraga-Silva RA, Piersigilli A, Tedgui A, Sordet-Dessimoz J, Astolfo A,  
429 Van der Donckt C, Modregger P, Stampanoni M, Segers P, Stergiopoulos N. Dissecting  
430 abdominal aortic aneurysm in ang ii-infused mice: Suprarenal branch ruptures and  
431 apparent luminal dilatation. *Cardiovasc. Res.* 2015;105:213-222  
432 7. Favreau JT, Nguyen BT, Gao I, Yu P, Tao M, Schneiderman J, Gaudette GR, Ozaki  
433 CK. Murine ultrasound imaging for circumferential strain analyses in the angiotensin  
434 ii abdominal aortic aneurysm model. *J. Vasc. Surg.* 2012;56:462-469  
435 8. Branchetti E, Poggio P, Sainger R, Shang E, Grau JB, Jackson BM, Lai EK, Parmacek  
436 MS, Gorman RC, Gorman JH, Bavaria JE, Ferrari G. Oxidative stress modulates  
437 vascular smooth muscle cell phenotype via ctgf in thoracic aortic aneurysm.  
438 *Cardiovasc. Res.* 2013;100:316-324  
439 9. Rateri DL, Davis FM, Balakrishnan A, Howatt DA, Moorlegghen JJ, O'Connor WN,  
440 Charnigo R, Cassis LA, Daugherty A. Angiotensin ii induces region-specific medial  
441 disruption during evolution of ascending aortic aneurysms. *Am. J. Pathol.*  
442 2014;184:2586-2595  
443 10. Chen X, Rateri DL, Howatt DA, Balakrishnan A, Moorlegghen JJ, Morris AJ, Charnigo  
444 R, Cassis LA, Daugherty A. Amlodipine reduces angii-induced aortic aneurysms and  
445 atherosclerosis in hypercholesterolemic mice. *PLoS ONE.* 2013;8:e81743  
446 11. Subramanian V, Moorlegghen JJ, Balakrishnan A, Howatt DA, Chishti AH, Uchida  
447 HA. Calpain-2 compensation promotes angiotensin ii-induced ascending and  
448 abdominal aortic aneurysms in calpain-1 deficient mice. *PLoS ONE.* 2013;8:e72214  
449 12. Zhang X, Thatcher SE, Rateri DL, Bruemmer D, Charnigo R, Daugherty A, Cassis  
450 LA. Transient exposure of neonatal female mice to testosterone abrogates the sexual  
451 dimorphism of abdominal aortic aneurysms. *Circ. Res.* 2012;110:e73-e85  
452 13. Fu X-m, Yamawaki-Ogata A, Oshima H, Ueda Y, Usui A, Narita Y. Intravenous  
453 administration of mesenchymal stem cells prevents angiotensin ii-induced aortic  
454 aneurysm formation in apolipoprotein e-deficient mouse. *J Transl Med.* 2013;11:175-  
455 175  
456 14. Rateri DL, Moorlegghen JJ, Balakrishnan A, Owens AP, Howatt DA, Subramanian V,  
457 Poduri A, Charnigo R, Cassis LA, Daugherty A. Endothelial cell-specific deficiency  
458 of ang ii type 1a receptors attenuates ang ii-induced ascending aortic aneurysms in ldl  
459 receptor<sup>-/-</sup> mice. *Circ. Res.* 2011;108:574-581  
460 15. McGavin MD, Zachary JF. *Pathologic basis of veterinary disease, 4th edition.*  
461 Missouri: Mosby Elsevier; 2007.

- 462 16. Trachet B, Fraga-Silva RA, Londono FJ, Swillens A, Stergiopoulos N, Segers P.  
463 Performance comparison of ultrasound-based methods to assess aortic diameter and  
464 stiffness in normal and aneurysmal mice. *PLoS ONE*. 2015;10:e0129007
- 465 17. Cotrufo M, Corte AD, De Santo LS, Quarto C, De Feo M, Romano G, Amarelli C,  
466 Scardone M, Di Meglio F, Guerra G, Scarano M, Vitale S, Castaldo C, Montagnani S.  
467 Different patterns of extracellular matrix protein expression in the convexity and the  
468 concavity of the dilated aorta with bicuspid aortic valve: Preliminary results. *J Thor*  
469 *Card Surg*. 2005;130:504.e501-504.e509
- 470 18. Bissell MM, Hess AT, Biasioli L, Glaze SJ, Loudon M, Pitcher A, Davis A,  
471 Prendergast B, Markl M, Barker AJ, Neubauer S, Myerson SG. Aortic dilation in  
472 bicuspid aortic valve disease: Flow pattern is a major contributor and differs with  
473 valve fusion type. *Circulation: Cardiovascular Imaging*. 2013;6:499-507
- 474 19. Tadros TM, Klein MD, Shapira OM. Ascending aortic dilatation associated with  
475 bicuspid aortic valve: Pathophysiology, molecular biology, and clinical implications.  
476 *Circulation*. 2009;119:880-890
- 477 20. Zhou Y-Q, Zhu S-N, Foster FS, Cybulsky MI, Henkelman RM. Aortic regurgitation  
478 dramatically alters the distribution of atherosclerotic lesions and enhances  
479 atherogenesis in mice. *Arterioscler. Thromb. Vac. Biol*. 2010;30:1181-1188
- 480 21. Atkins S, Cao K, Rajamannan N, Sucosky P. Bicuspid aortic valve hemodynamics  
481 induces abnormal medial remodeling in the convexity of porcine ascending aortas.  
482 *Biomech Model Mechanobiol*. 2014;13:1209-1225
- 483 22. Cotrufo M, Della Corte A. The association of bicuspid aortic valve disease with  
484 asymmetric dilatation of the tubular ascending aorta: Identification of a definite  
485 syndrome. *Journal of Cardiovascular Medicine*. 2009;10:291-297
- 486 23. Durdu S, Deniz GC, Balci D, Zaim C, Dogan A, Can A, Akcali KC, Akar AR.  
487 Apoptotic vascular smooth muscle cell depletion via bcl2 family of proteins in human  
488 ascending aortic aneurysm and dissection. *Cardiovascular Therapeutics*. 2012;30:308-  
489 316
- 490 24. Lesauskaite V, Tanganelli P, Sassi C, Neri E, Diciolla F, Ivanoviene L, Epistolato  
491 MC, Lalinga AV, Alessandrini C, Spina D. Smooth muscle cells of the media in the  
492 dilatative pathology of ascending thoracic aorta: Morphology, immunoreactivity for  
493 osteopontin, matrix metalloproteinases, and their inhibitors. *Hum. Pathol.*;32:1003-  
494 1011
- 495 25. van Thiel BS, van der Pluijm I, te Riet L, Essers J, Danser AHJ. The renin-  
496 angiotensin system and its involvement in vascular disease. *Eur. J. Pharmacol*.  
497 2015;763, Part A:3-14
- 498 26. Abdulkareem N, Smelt J, Jahangiri M. Bicuspid aortic valve aortopathy: Genetics,  
499 pathophysiology and medical therapy. *Interactive CardioVascular and Thoracic*  
500 *Surgery*. 2013;17:554-559
- 501 27. Wolinsky H, Glagov S. Structural basis for the static mechanical properties of the  
502 aortic media. *Circ. Res*. 1964;14:400-413
- 503 28. Shadwick RE. Mechanical design in arteries. *J. Exp. Biol*. 1999;202:3305-3313
- 504 29. Trachet B, Bols J, Degroote J, Verheghe B, Stergiopoulos N, Vierendeels J, Segers P.  
505 An animal-specific fsi model of the abdominal aorta in anesthetized mice *Ann*.  
506 *Biomed. Eng*. 2015;43:1298-1309
- 507 30. Trachet B, Fraga-Silva RA, Jacquet P, Stergiopoulos N, Segers P. Incidence, mortality  
508 and confounding factors for aaa detection in angiotensin ii-infused mice: A meta-  
509 analysis. *Cardiovasc. Res*. 2015;108:159-170

510

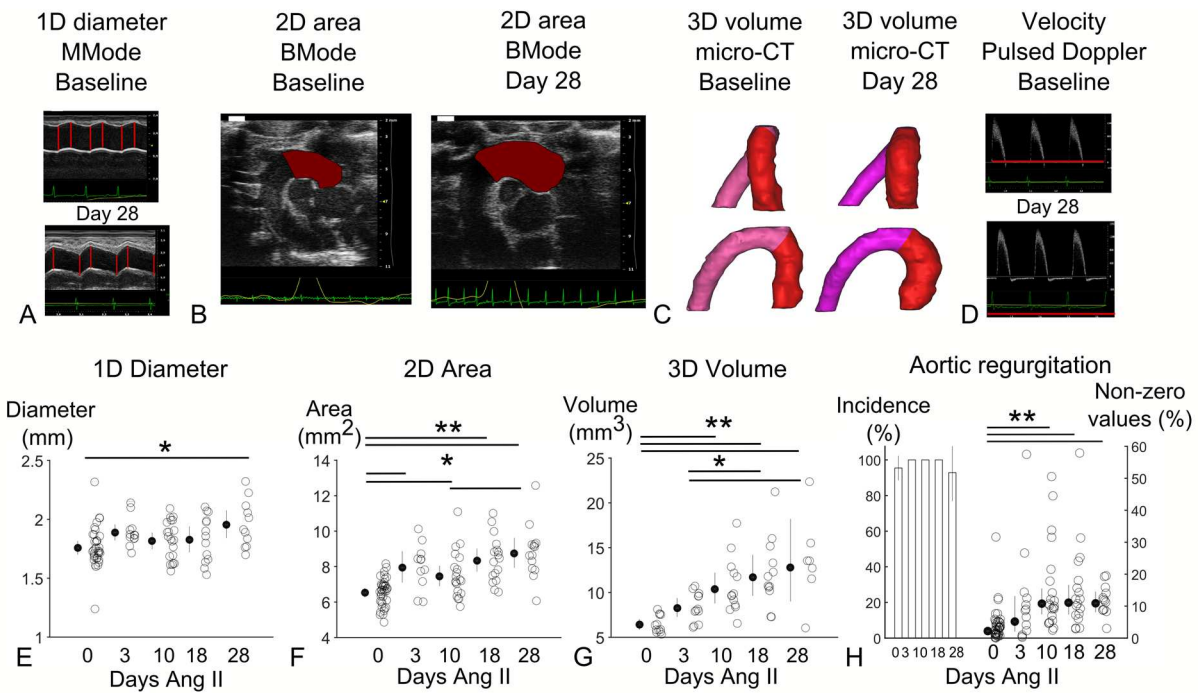
511 **Significance**

512 Angiotensin II-infused ApoE<sup>-/-</sup> mice are an important mouse model for aortic  
513 aneurysm, but the anatomy of their ascending aneurysms has never been fully  
514 understood due to inherent limitations in the currently available small animal imaging  
515 technology. In this work we combined in vivo imaging with high-resolution ex vivo  
516 imaging and image-guided histology to provide an unprecedented insight into the  
517 pathophysiology and the temporal evolution of these lesions. In the short term our  
518 aim is to improve the basic knowledge of how ascending aortic aneurysms form in  
519 mice, and to serve as a valuable source of insight for past and future studies that rely  
520 on this popular mouse model. In the long term we believe that our research will  
521 improve future pre-clinical aneurysm research and that it will contribute to enhance  
522 our understanding of the initiation of ascending aortic aneurysm in humans.

523



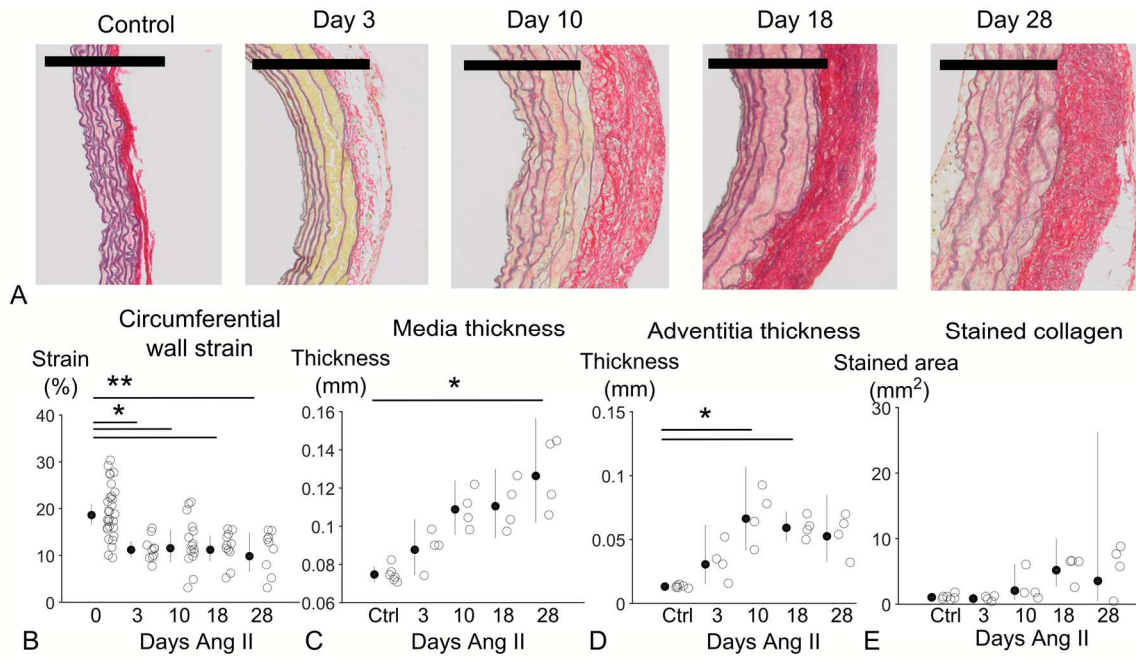
524 **Figure legends**



525

526 **Figure 1. In vivo changes in aortic size and aortic regurgitation severity.** Top:  
 527 Representative images of in vivo acquisition of size and blood velocity of the ascending aorta  
 528 with 1D MMode (a), 2D BMode (b), 3D micro-CT (c) and Pulsed Doppler (d). Measured  
 529 regions are shown in red. Scale bar represents 1 mm. Scatter plots in panels e–g show the  
 530 measurements at different time points (1D: MMode, 2D: BMode, 3D: micro-CT), as well as  
 531 the mean and the 95% confidence interval (calculated in the normal domain after a log  
 532 transformation). In panel h the bar plots (on the left) show the incidence of aortic  
 533 regurgitation for each time point ( $100 \cdot n_1/n_2$ , with  $n_1$  all mice that have aortic regurgitation at  
 534 that time point and  $n_2$  all mice measured at that time point) while the scatter plots (on the  
 535 right) show the amount of regurgitation in those mice where aortic regurgitation was present  
 536 (non-zero values). \*:  $p < 0.05$ , \*\*:  $p < 0.001$ .

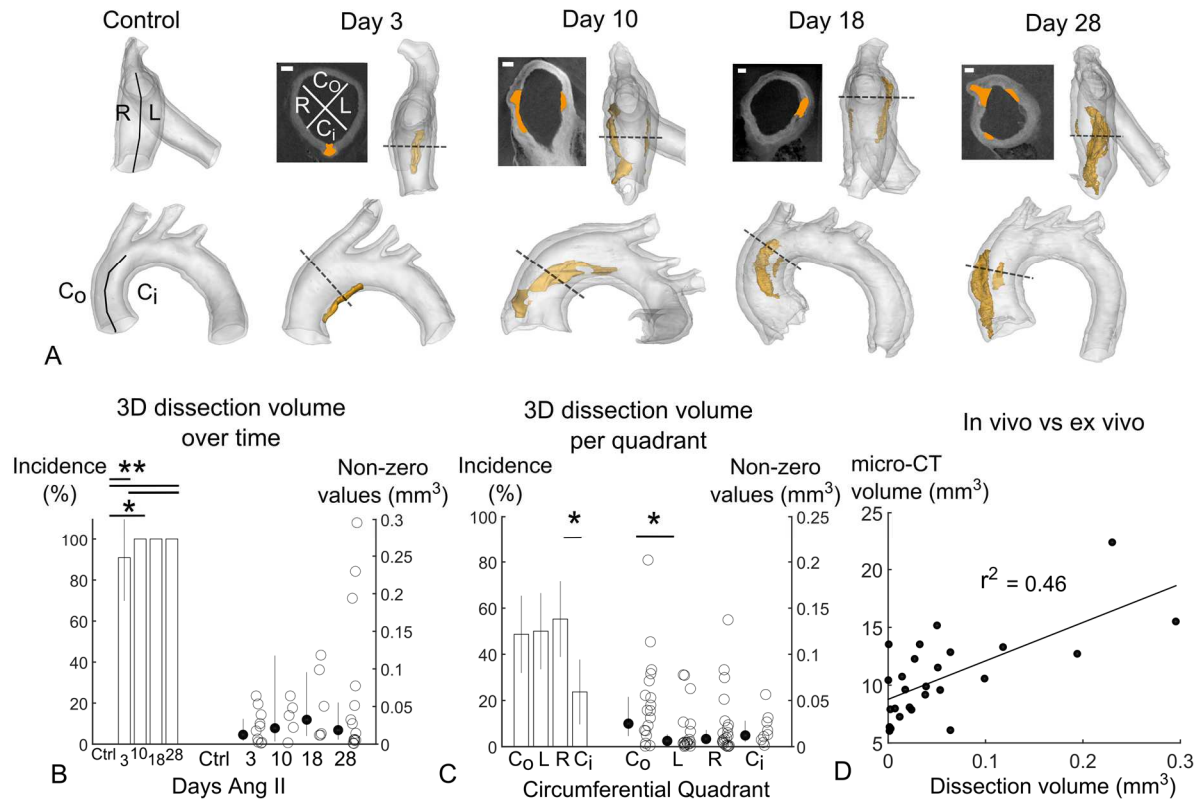
537



538  
 539  
 540  
 541  
 542  
 543  
 544  
 545  
 546

**Figure 2. Spatial and temporal variation of aortic wall properties and morphology.** Top: Representative Sirius Red – Miller stains showing the aortic wall matrix composition at different time points. Collagen in red, elastin in grey. Scale bar represents 200  $\mu\text{m}$ . Scatter plots in panels **b – e** show the evolution of circumferential strain (**b**), intima-media thickness (**c**), adventitia thickness (**d**) and collagen deposition (**e**) over time. The mean and 95% confidence interval are calculated in the normal domain after a log transformation. 3-4 stains, each obtained by image-guided histology, were averaged per animal to account for intra-subject variation. \*:  $p < 0.05$ , \*\*:  $p < 0.001$ .

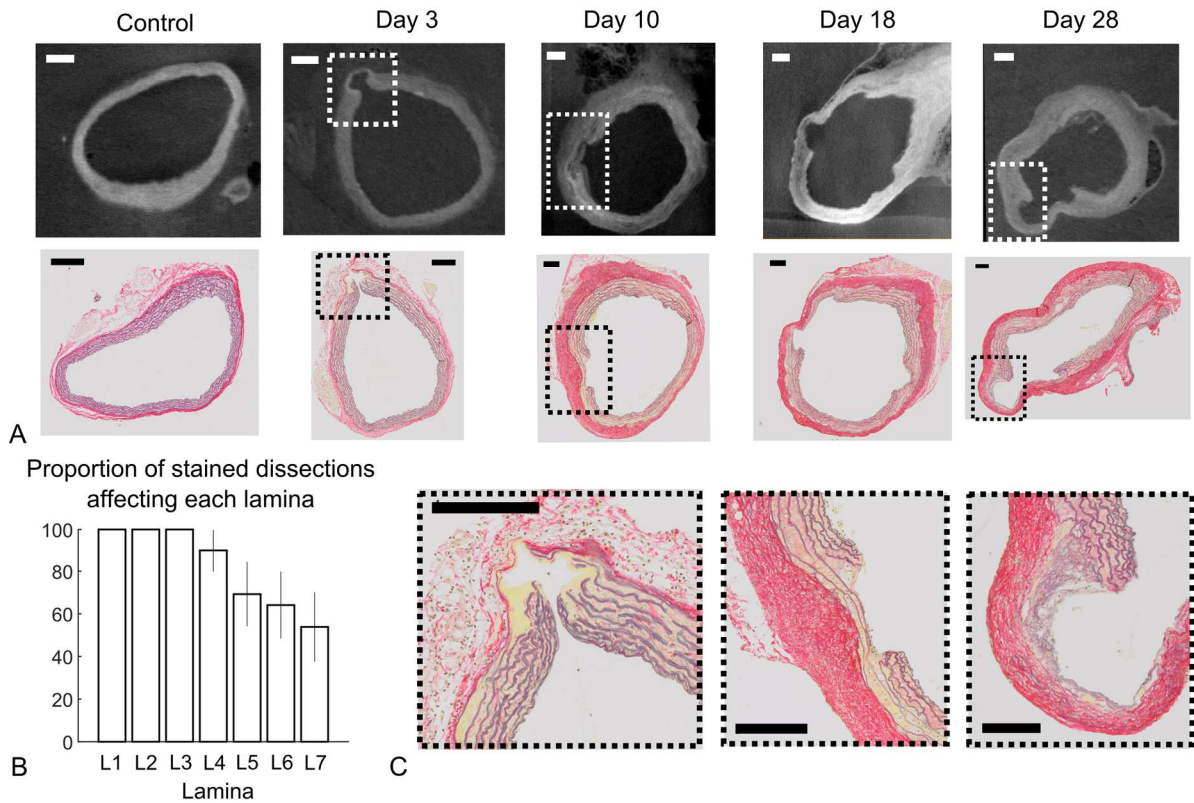
547



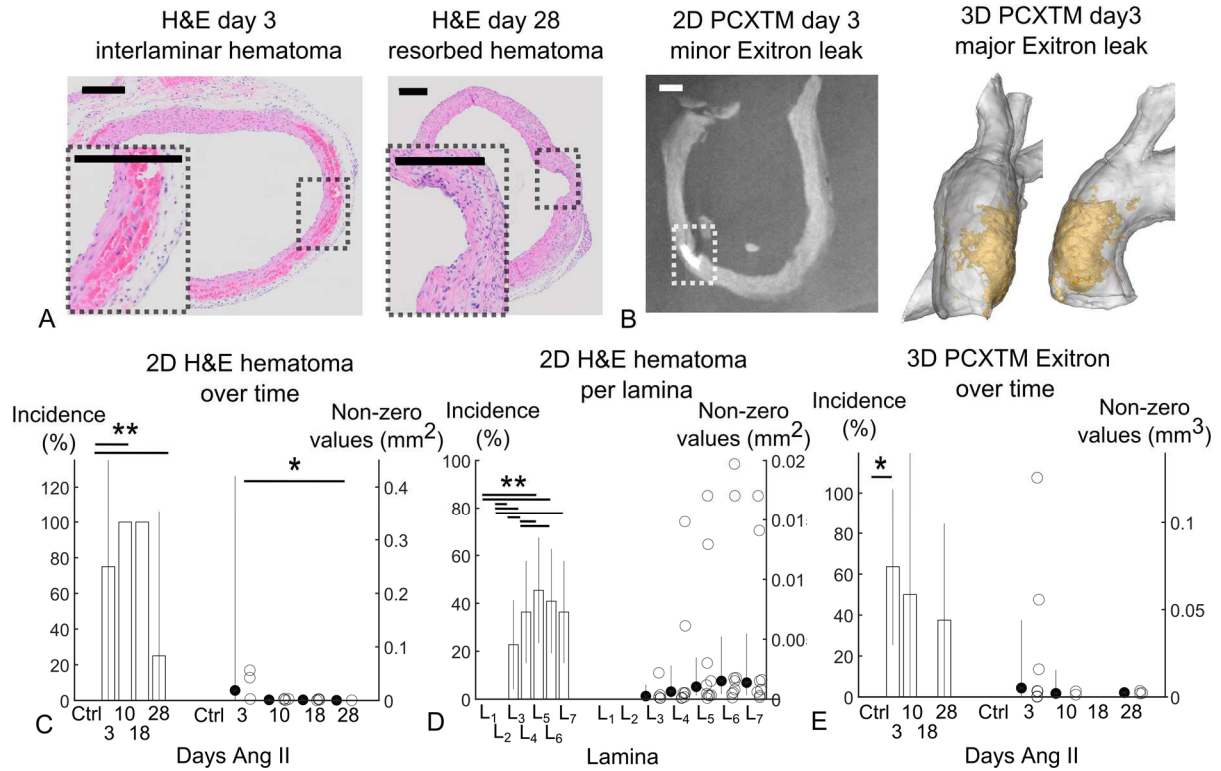
548  
549  
550  
551  
552  
553  
554  
555  
556  
557  
558  
559  
560  
561

**Figure 3. 3D PCXTM imaging of focal dissections.** **a.** 2D and segmented 3D representation of the aortic arch at different time points. Dissections in orange. R: right quadrant, L: left quadrant, C<sub>o</sub>: outer convex quadrant, C<sub>i</sub>: inner convex quadrant. Scale bar represents 200 μm. **b.** PCXTM-based dissection volume over time. The bar plots (on the left) show the incidence of aortic dissections for each time point (100\*n1/n2, with n1 all mice that have a dissection at that time point and n2 all mice measured at that time point) while the scatter plots (on the right) show the volume of the dissections for the non-zero values (n1). **c.** PCXTM-based dissection volume over the circumference. The bar plots (on the left) show the incidence of aortic dissections in each quadrant while the scatter plots (on the right) show the volume of the dissections for the non-zero values. **d.** Scatter plot showing the relation between lumen volume obtained with in vivo micro-CT (Figure 1c, red volume) and dissection volume obtained with ex vivo PCXTM (Figure 3a, orange volume). \*: p<0.05, \*\*: p<0.001.

562

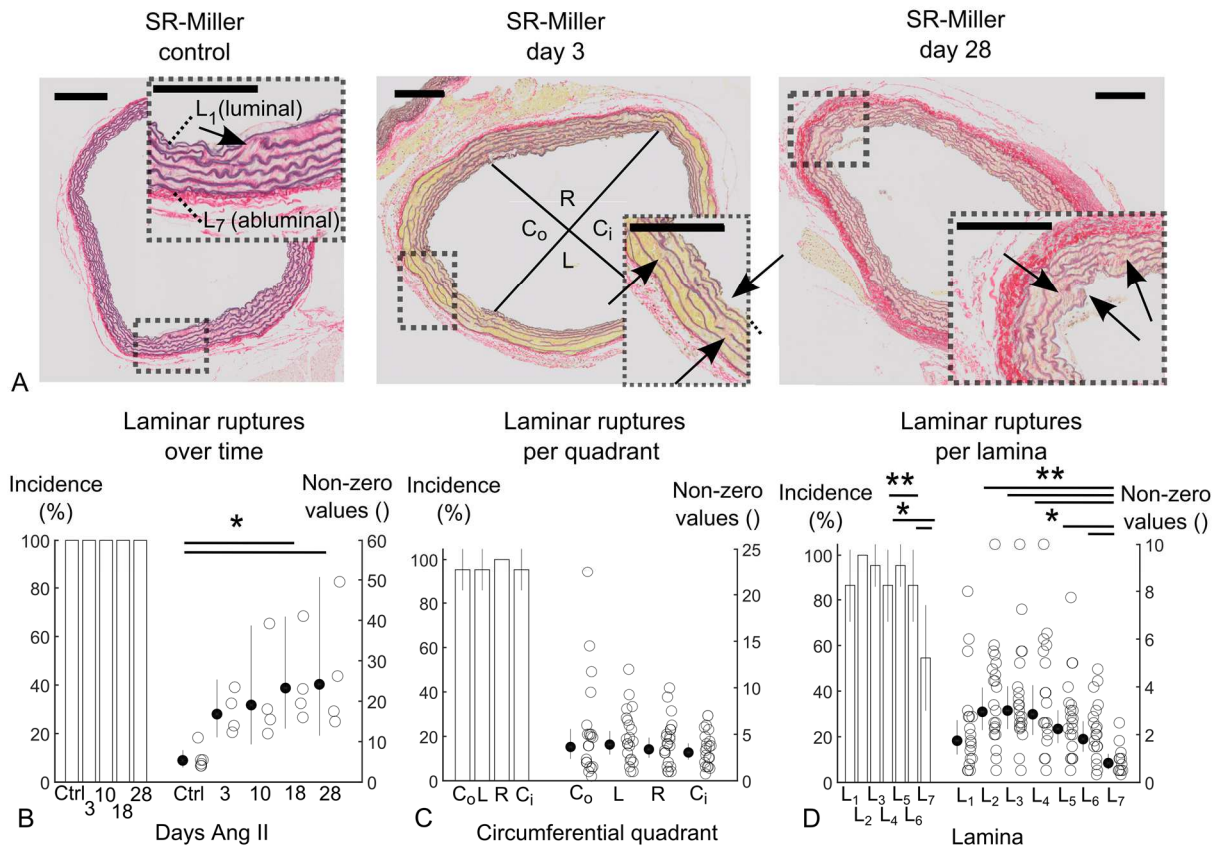


563  
 564  
 565  
 566  
 567  
 568  
 569  
 570  
 571  
 572  
 573  
 574  
 575



576  
 577  
 578  
 579  
 580  
 581  
 582  
 583  
 584  
 585  
 586  
 587  
 588  
 589

**Figure 5. Spatial and temporal distribution of interlamellar hematoma.** **a.** representative Hematoxin-Eosin (H&E) stains after 3 and 28 days of angiotensin II infusion. Scale bar represents 200  $\mu$ m. **b.** Left: 2D PCXTM image showing how Exitron (white contrast agent, injected in vivo prior to sacrifice) leaks in between the laminae through an intimal tear. Right: 3D representation of a major Exitron leakage (in orange) that has percolated into the tunica media (in transparent white). **c.** Change in hematoma area over time. The bar plots (on the left) show the incidence of hematoma on the analyzed stains at each time point while the scatter plots (on the right) show the area of the hematoma for non-zero values. **d.** Change in hematoma area per lamina. 3-4 stains, each obtained by image-guided histology, were averaged per animal to account for intra-subject variation. **e.** Exitron volume penetrating into the tunica media over time. \*:  $p < 0.05$ , \*\*:  $p < 0.001$ .



590  
 591  
 592  
 593  
 594  
 595  
 596  
 597  
 598  
 599  
 600

**Figure 6. Spatial and temporal distribution of laminar ruptures.** **a.** Representative SR-Miller stains showing elastic laminae ruptures after saline infusion (left) and after 3 (middle) and 28 (right) days of angiotensin II infusion. Laminar ruptures that were part of focal dissections were not taken into account to avoid double reporting. Scale bar represents 200  $\mu$ m. **b.** Laminar ruptures over time. The bar plots (on the left) show the incidence of laminar ruptures at each time point while the scatter plots (on the right) show the number of ruptures for each time point. **c.** Circumferential variation of laminar ruptures. **d.** Change in laminar ruptures per lamina. L1: luminal (intima), L7: abluminal (adjacent to adventitia). 3-4 stains, each obtained by image-guided histology, were averaged per animal to account for intra-subject variation. \*:  $p < 0.05$ , \*\*:  $p < 0.001$ .

601

602 **Ascending aortic aneurysm in angiotensin II- infused**  
603 **mice: formation, progression and the role of focal**  
604 **dissections**

605  
606

607 **Supplementary Data:**  
608 **Detailed Materials and Methods**

609  
610  
611

612 Bram Trachet<sup>1,2</sup>, Alessandra Piersigilli<sup>3,4</sup>, Rodrigo A. Fraga-Silva<sup>1</sup>, Lydia Aslanidou<sup>1</sup>,  
613 Jessica Sordet-Dessimoz<sup>5</sup>, Alberto Astolfo<sup>6</sup>, Marco F.M. Stampanoni<sup>6,7</sup>, Patrick  
614 Segers<sup>2</sup>, Nikolaos Stergiopoulos<sup>1</sup>

615  
616  
617

618 <sup>1</sup> Institute of Bioengineering, Ecole Polytechnique Fédérale de Lausanne, Lausanne,  
619 Switzerland

620 <sup>2</sup> IBiTech - bioMMeda, Ghent University-iMinds Medical IT, Ghent, Belgium

621 <sup>3</sup> School of Life Sciences, PTEC GE, Ecole Polytechnique Fédérale de Lausanne, Lausanne,  
622 Switzerland

623 <sup>4</sup> Institute of Animal Pathology, Vetsuisse Faculty, University of Bern, Bern, Switzerland

624 <sup>5</sup> Histology Core Facility, Ecole Polytechnique Fédérale de Lausanne, Lausanne, Switzerland

625 <sup>6</sup> Swiss Light Source, Paul Scherrer Institut, Villigen, Switzerland

626 <sup>7</sup> Institute for Biomedical Engineering, University and ETH Zürich, Zürich, Switzerland

627  
628

629 **Animal model.** All the procedures were approved by the Ethical Committee of Canton  
630 Vaud, Switzerland (EC 2647.2) and performed according to the guidelines from  
631 Directive 2010/63/EU of the European Parliament on the protection of animals used  
632 for scientific purposes. Applying the 3R principle (replace, reduce, refine), we used the  
633 same animals for a parallel study on abdominal aortic aneurysm formation (yet to be  
634 published). The incidence of ascending aneurysms is the same for ApoE<sup>-/-</sup> and regular  
635 C57Bl/6J mice<sup>1</sup>, while the incidence of abdominal aortic aneurysms is significantly  
636 higher for ApoE<sup>-/-</sup> mice<sup>2</sup>. Therefore male ApoE<sup>-/-</sup> mice on a C57Bl/6J background were  
637 purchased from Janvier (Saint Berthevin, France). At the age of 12 weeks, n=47 mice  
638 were implanted with a 200 µl osmotic pump (model Alzet 2004; Durect Corp, Cupertino,  
639 CA), filled with a solution of angiotensin II in saline (Bachem, Bubendorf, Switzerland)  
640 as previously described<sup>3</sup>. At the age of 14 weeks, n= 6 control mice were implanted  
641 with a 200 µl osmotic pump delivering saline. Each pump infused angiotensin II at  
642 1000 ng/kg/min<sup>4</sup>. Water and regular mouse diet were available *ad libitum* and animals  
643 were observed daily after the osmotic pump implantation. Aneurysm onset was  
644 instrumentally verified as described later.

645 **Sample size.** In total, N= 47 angiotensin II-infused animals and n= 6 controls  
646 underwent in vivo imaging. N= 35 out of the 47 angiotensin II-infused animals were  
647 included in the long-term in vivo imaging part of the study. N=13 of these animals died  
648 with hemothorax (n=7) or hemoabdomen (n=6) during the study. The remaining  
649 animals were sacrificed after 10 (n=4), 18 (n=5) and 28 (n=13) days of angiotensin II  
650 infusion (Figure 1). These animals were all scanned with ultrasound prior to pump  
651 implantation and at each intermediate time point. A subsample (n=11/35) was followed-  
652 up with micro-CT at baseline and intermediate time points. Additional micro-CT scans  
653 were obtained at intermediate time points if mice from the original micro-CT group died  
654 or were sacrificed. This resulted in n=13 micro-CT scans at day10, n=12 at day 18 and  
655 n=7 at day 28.

656 N=12/47 angiotensin II–infused animals were included in the short-term in vivo imaging  
657 part of the study. These were sacrificed after 3 days of Ang II infusion. The day 3  
658 animals were all scanned with ultrasound prior to pump implantation and with  
659 ultrasound and micro-CT prior to sacrifice. More mice were sacrificed in the short-term  
660 study because at this early stage of the disease the differences with controls were  
661 expected to be smaller. N=1 animal of this group died with hemothorax after in vivo  
662 imaging at day 3, but prior to sacrifice.

663 In total n=48/53 ascending aortic samples (n=30/33 samples from sacrificed Ang II-  
664 infused animals, n=12/14 samples from Ang II-infused animals that succumbed to  
665 hemothorax or hemoabdomen, and n=6/6 samples from saline-infused animals) were  
666 imaged with PCXTM. Five samples could not be analyzed ex vivo, either because the  
667 sample was damaged during dissection (n=3) or because too much time had passed  
668 between death from aneurysm rupture and tissue collection (n=2). The operator was  
669 blinded during all data analysis.

670 For ultrasound, micro-CT and PCXTM each animal represents one data point. For  
671 image-guided histology a representative, randomized sample of n=4 animals was  
672 analyzed at each time point. The goal of image-guided histology was to describe the  
673 biological variation within the lesions. If a lesion was visible on PCXTM, image-guided  
674 staining targeted 2-3 regions of the lesion in order to capture its start, middle and end.  
675 For each animal the final data point represents the mean value of these regions, in  
676 order to account for intra-subject variability. If no lesion was visible (e.g. saline-infused  
677 controls) 2 regions were analyzed per sample.

678



679 **In vivo imaging.** During both ultrasound and micro-CT imaging, animals were  
680 anesthetized with 1.5% isoflurane. Ultrasound imaging was performed with a high-  
681 frequency ultrasound device (Vevo 2100, VisualSonics, Toronto, Canada) using a  
682 linear array probe (MS 550D, frequency 22-55 MHz). Heart rate and respiration rate  
683 were kept constant, and the temperature of the ultrasound table was kept at 40 degrees  
684 during the experiment. Blood flow in the ascending aorta was visualized by Color  
685 Doppler measurements of the aortic arch and Pulsed Doppler measurements at the  
686 level of the ascending aorta (just downstream the aortic valve) and the descending  
687 aorta (just distal to the bifurcation of the left subclavian artery). An example of the  
688 placement of the Pulsed Doppler probe is shown in Figure Id. Diameter distension  
689 waveforms were acquired using radiofrequency (RF) MMode at the ascending aorta,  
690 and BMode images of the aortic arch were obtained in longitudinal view. The  
691 ultrasound imaging protocol was limited in time for ethical reasons (duration of  
692 anesthesia). If measurements did not meet sufficient quality, e.g. due to shadows or  
693 reverberations, they were repeated as long as the available time frame permitted so.  
694 Images that were still of insufficient quality were excluded from further analysis.  
695 Animals followed up in vivo with micro-CT were injected in the lateral tail vein with 4  
696  $\mu$ l/gram body weight of ExiTron nano 12000 (Miltenyi Biotec, Bergisch Gladbach,  
697 Germany) as previously described<sup>5</sup>. After the experiments, mice were anesthetized  
698 by Ketamine/Xylazine and the sacrifice was resolved following tissue collection.

699 **PCXTM imaging.** After sacrifice, the aorta was flushed in situ by transcardiac  
700 perfusion with phosphate buffered saline (PBS, pH 7.4) through the left ventricle. The  
701 thoracic aorta was carefully excised and samples were fixated by immersion in  
702 freshly prepared 4% paraformaldehyde (PFA) at 4°C temperature for 24 hours. In  
703 animals that succumbed to transmural aortic dissection, the aorta was collected  
704 (without flushing) as soon as possible after finding them dead. N=48 collected  
705 samples were scanned at the TOMCAT beamline of the Swiss Light Source, Paul  
706 Scherrer Institut, Villigen, Switzerland. Samples were embedded in 1% agarose gel  
707 to stabilize them. The imaging setup consists in two gratings (phase and absorption)  
708 with 3.98 and 2  $\mu$ m pitch respectively, positioned at a relative distance of 121 mm. It  
709 corresponds to the third fractional Talbot distance at 25 keV. A total of 1441  
710 projections have been acquired over 180 degrees rotations for each of the 5 phase  
711 grating steps<sup>5</sup>.

712 **Lesion terminology.** Throughout the manuscript, a consistent terminology has been  
713 used to avoid confusion between different types of lesions that were observed in the  
714 aortic wall.

715 *Laminar rupture:* a discontinuity of a single elastic aortic lamina (i.e. one of the seven  
716 lamellar layers) due to breaks in single lamellar units in the tunica media, as observed  
717 on the Miller stain.

718 *Interlaminar hematoma:* a local entrapment of free erythrocytes that is confined within  
719 the tunica media, between 2 laminae, as observed on the H&E stain.

720 *Dissection (or tear):* a discontinuity of the tunica media with a depth of 3 or more  
721 consecutive laminae, as observed on the Miller stain. On PCXTM images, dissections  
722 were identified as a discontinuity of the tunica media in which the luminal gap  
723 corresponds to at least 10% of the wall thickness in an unchanged (normal) area.

724 *Transmural dissection:* A full thickness rupture of the aortic wall (including tunica media  
725 and tunica adventitia) that leads to hemorrhage and death of the animal by  
726 hypovolemic shock.

727

728 **Image processing.** Ultrasound Pulsed Doppler waveforms were traced within a  
729 custom-made environment platform in Matlab (Mathworks, Natick, MA) and the  
730 average of three different waveforms was computed. The entity of aortic regurgitation  
731 in the ascending aorta was subsequently determined as the (dimensionless) ratio of  
732 the cumulative integral of negative velocity over the total cumulative integral of positive  
733 and negative velocity, both of which were quantified via numerical integration over the  
734 flow velocity waveform. A custom-written, Matlab-based application was used to obtain  
735 the aortic diameter distension from the 1D RF MMode data. For each diameter  
736 measurement, 3 cardiac cycles were selected and plotted as a reference for semi-  
737 automatic wall segmentation as previously described <sup>6</sup>. The circumferential cyclic  
738 Green-Lagrange strain (eq. 1) was calculated as a measure for aortic compliance  
739 under the assumption of uniform strain around the vessel <sup>7</sup>.

$$740 \quad \text{Circ.strain} = \frac{1}{2} \left[ \left( \frac{D_{sys}}{D_{dia}} \right)^2 - 1 \right] * 100\% \quad (\text{eq. 1})$$

741 2D Ultrasound BMode images were analyzed using the built-in Vevo tracing software.  
742 Area measurements were measured in a longitudinal view, similar to the method  
743 proposed by Rateri *et al* <sup>1</sup>. BMode measurements include the ascending aspect of the  
744 aorta from (but not including) the aortic valve until (but not including) the branching of  
745 the brachiocephalic trunk (Figure 1a, 1b). All reconstructed 3D datasets (in vivo micro-  
746 CT as well as PCXTM) were semi-automatically segmented into 3D models using the  
747 commercial software package Mimics (Materialise, Leuven, Belgium). Segmentation  
748 of the in vivo micro-CT data allowed for quantification of the 3D volume of the  
749 pressurized, blood-filled lumen. Volume measurements included the ascending portion  
750 of the aorta, just before the branching of the brachiocephalic trunk (Figure 1a, 1b).  
751 Segmentation of ex vivo PCXTM data allowed for 3 dimensional quantification of the  
752 size of focal dissections. Volume measurements of the dissections quantified the  
753 volume of the loss of substance in the tunica media, and thus required extrapolation of  
754 the damaged tunica intima (Figure 3a). In order to describe the topography of the  
755 circumferential variation of these dissections the ascending aorta was subdivided into  
756 4 quadrants representing the outer convex, left, right and inner convex aspect of the  
757 ascending aorta (Figure 3). For each quadrant the total volume of all (parts of)  
758 dissections observed in it was computed.

759  
760 **PCXTM-guided histology.** After PCXTM scanning, the samples were fixated as  
761 mentioned above, processed and embedded in paraffin according to standard  
762 histological procedures. 4 μm thick paraffin sections were carefully compared to the  
763 corresponding PCXTM images under a Leica DM750 bright field microscope to spot  
764 the exact location of dissections. Selected slides were stained with Haematoxylin-  
765 Eosin (H&E) to assess general morphology. Miller stain and Sirius red F3B (CI35782,  
766 Direct red 80) were combined to specifically highlight elastic fibers and collagen on the  
767 same section. Prussian Blue, which is a specific stain for iron, confirmed the  
768 cytoplasmic hemoglobin and hemosiderin within macrophages (hemosiderophages) at  
769 sites of hematoma resorption. In order to confirm the contribution of smooth muscle  
770 cells apoptosis to the progressive degeneration of the media, sections obtained from  
771 controls and angiotensin II-infused mice at different time points were co-stained for  
772 cleaved caspase 3 and α-SMA on the same slice using the Ventana Discovery XT.  
773 Dewaxed and rehydrated paraffin sections were pretreated with heat using the CC1  
774 solution under standard conditions (36 minutes). The primary antibody rabbit anti  
775 cleaved caspase-3 (Asp175, Cell Signaling) diluted 1:100 in 1% BSA in PBS was

776 incubated 1 hour at 37°C. Detection was performed with the secondary rabbit  
777 OmniMAP and the DAbMap revelation kit (Roche Diagnostics, Rotkreuz, Switzerland).  
778 Antibodies were eluted using heat then the rabbit anti  $\alpha$ -SMA (clone E184, Abcam)  
779 diluted 1:200 in 1% BSA in PBS was incubated 1 hour at 37°C. After incubation with a  
780 donkey  $\alpha$ -rabbit biotin antibody diluted 1:500 in 1% BSA in PBS (Jackson  
781 ImmunoResearch Laboratories), chromogenic revelation was performed with a  
782 BlueMap kit (Roche Diagnostics, Rotkreuz, Switzerland).

783 **Histology image processing.** All slides were photographed using an automated slide  
784 scanner (VI20-L100, Olympus) and analyzed using a dedicated plug-in in the open  
785 source software Fiji<sup>8</sup>. All slides were carefully compared to the stack of 2D PCXTM  
786 images as well as the segmented 3D PCXTM vessel in order to determine the  
787 orientation of the slide. Each intersection was subsequently subdivided into one of four  
788 quadrants. Outer convex, inner convex, left and right aortic quadrants were determined  
789 based on the exact match between 2D PCXTM and image-guided histology. Combined  
790 thickness of the tunica intima and media as well as thickness of the tunica adventitia  
791 were measured on combined SR-Miller stains. In order to account for local variations  
792 in thickness, 32 measurements were made for each scanned slide: 4 measurements  
793 per quadrant for both the intima-media and the adventitia. Furthermore the number  
794 and size (in mm<sup>2</sup>) of focal dissections was quantified on SR-Miller stains for each  
795 quadrant. Similar to the PCXTM measurements, the size of the lesions was quantified  
796 as the area of loss of substance (dissection) in the wall. The number of laminar ruptures  
797 was quantified for each elastic layer and for each quadrant on SR-Miller stains. In order  
798 to avoid double reporting of data, laminar ruptures that formed part of a focal dissection  
799 (i.e. loss of continuity of three consecutive luminal laminae) were not included in the  
800 count. Finally, the size of interlaminar hematomas was quantified on Haematoxylin-  
801 Eosin (H&E) sections as the area occupied by extraluminal free erythrocytes. This area  
802 was computed for each quadrant and outside each lamina. Laminae were ordered from  
803 the luminal (L1) to the abluminal (L7) side. If less than 7 laminae were present, no  
804 values were counted for L7. If more than 7 laminae were present, results for L8 were  
805 added to those of L7. Given the low variation in lamellae in between mice<sup>9</sup>, both effects  
806 were rare and cancelled each other out. A semi-quantitative measurement of collagen  
807 deposition was performed by image analysis (ImageJ). The image was split into its  
808 RGB channels and the Green channel was used for image analysis. The aortic wall  
809 was segmented manually and the same threshold was used for all analyzed images.

810 **Statistics.** For all in vivo experiments the baseline scans (and not the saline-infused  
811 control animals) served as control data. All data from in vivo experiments were first  
812 transformed from the lognormal to the normal domain by a log transformation. Log-  
813 transformed data were tested for normality by the Shapiro-Wilk parametric hypothesis  
814 test and visually checked for adherence to the x=y reference line on a normal  
815 probability plot. Equal variance was tested with Bartlett's test. The conditions for  
816 parametric testing were met for all in vivo variables and therefore their variation in  
817 between time points was calculated using a one-way Anova analysis (Table II). Post-  
818 hoc pairwise comparisons were performed using a Bonferroni correction. A p-value of  
819 0.05 was considered significant (\*), and a p-value of 0.001 was considered highly  
820 significant (\*\*). The mean and 95% confidence interval were first calculated in the  
821 normal domain and then back-calculated to the original scale. Therefore geometric  
822 means and asymmetric confidence intervals are reported in the Figures and Tables.

823 For the ex vivo experiments (PCXTM and histology), 6 saline-infused mice (and not  
824 the baseline data, which were not available ex vivo) served as controls. For the ex vivo  
825 measurements we reported the incidence (Table II) and the variation of magnitude  
826 within non-zero values (Table I) separately.

827 Incidence was defined as  $100 \cdot n_1/n_2$ , with  $n_1$  all mice that have a non-zero value at  
828 that time point (or quadrant, or lamina) and  $n_2$  all mice that were measured at that time  
829 point (or quadrant, or lamina). Incidence rates were reported as bar plots with 95%  
830 confidence intervals. The 95% confidence interval was calculated based on a student's  
831 distribution and  $SEM = \sqrt{p \cdot (1-p)/n}$ . For each analyzed variable the variation of the  
832 incidence values in between time points, in between quadrants and in between layers  
833 was calculated using a chi-square test (Table II). Pairwise comparisons were  
834 performed using a Tukey's HSD multiple comparisons test. A p-value of 0.05 was  
835 considered significant (\*), and a p-value of 0.001 was considered highly significant (\*\*).

836 The non-zero values from ex vivo experiments (PCXTM and histology) had fewer  
837 measurements per time point than the in vivo measurements. There were too few  
838 samples per time point to ascertain normality and the Bartlett test showed significant  
839 differences in variance between time points, even after log transformation. Therefore  
840 in this case a Kruskal-Wallis analysis was performed, followed by a post-hoc Dunn's  
841 test for pairwise comparisons. A p-value of 0.05 was considered significant (\*), and a  
842 p-value of 0.001 was considered highly significant (\*\*). For the analysis of ex vivo data  
843 in between circumferential quadrants and in between laminae the conditions for Anova  
844 analysis were met and a similar approach as for in vivo data was followed.

845

846

847 **References**

- 848 1. Rateri DL, Davis FM, Balakrishnan A, Howatt DA, Moorleghen JJ, O'Connor WN,  
849 Charnigo R, Cassis LA, Daugherty A. Angiotensin ii induces region-specific medial  
850 disruption during evolution of ascending aortic aneurysms. *Am. J. Pathol.*  
851 2014;184:2586-2595
- 852 2. Trachet B, Fraga-Silva RA, Jacquet P, Stergiopoulos N, Segers P. Incidence, mortality  
853 and confounding factors for aaa detection in angiotensin ii-infused mice: A meta-  
854 analysis. *Cardiovasc. Res.* 2015;108:159-170
- 855 3. Trachet B, Renard M, De Santis G, Staelens S, De Backer J, Antiga L, Loeys B,  
856 Segers P. An integrated framework to quantitatively link mouse-specific  
857 hemodynamics to aneurysm formation in angiotensin ii-infused apoe -/- mice. *Ann.*  
858 *Biomed. Eng.* 2011;39:2430-2444
- 859 4. Wang Y, Ait-Oufella H, Herbin O, Bonnin P, Ramkhelawon B, Taleb S, Huang J,  
860 Offenstadt G, Combadiere C, Renia L, Johnson JL, Tharaux P-L, Tedgui A, Mallat Z.  
861 Tgf-beta activity protects against inflammatory aortic aneurysm progression and  
862 complications in angiotensin ii-infused mice. *J. Clin. Invest.* 2010;120:422-432
- 863 5. Trachet B, Fraga-Silva RA, Piersigilli A, Tedgui A, Sordet-Dessimoz J, Astolfo A,  
864 Van der Donckt C, Modregger P, Stampanoni M, Segers P, Stergiopoulos N. Dissecting  
865 abdominal aortic aneurysm in ang ii-infused mice: Suprarenal branch ruptures and  
866 apparent luminal dilatation. *Cardiovasc. Res.* 2015;105:213-222
- 867 6. Trachet B, Fraga-Silva RA, Londono FJ, Swillens A, Stergiopoulos N, Segers P.  
868 Performance comparison of ultrasound-based methods to assess aortic diameter and  
869 stiffness in normal and aneurysmal mice. *PLoS ONE.* 2015;10:e0129007
- 870 7. Goergen CJ, Barr KN, Huynh DT, Eastham-Anderson JR, Choi G, Hedehus M,  
871 Dalman RL, Connolly AJ, Taylor CA, Tsao PS, Greve JM. In vivo quantification of  
872 murine aortic cyclic strain, motion, and curvature: Implications for abdominal aortic  
873 aneurysm growth. *J. Magn. Reson. Imaging.* 2010;32:847-858
- 874 8. Schindelin J, Arganda-Carreras I, Frise E, Kaynig V, Longair M, Pietzsch T, Preibisch  
875 S, Rueden C, Saalfeld S, Schmid B, Tinevez J-Y, White DJ, Hartenstein V, Eliceiri K,  
876 Tomancak P, Cardona A. Fiji - an open source platform for biological image analysis.  
877 *Nat. Methods.* 2012;9:10.1038/nmeth.2019
- 878 9. Goergen CJ, Li H-H, Francke U, Taylor CA. Induced chromosome deletion in a  
879 williams-beuren syndrome mouse model causes cardiovascular abnormalities. *J. Vasc.*  
880 *Res.* 2011;48:119-129

881

882

883

884